SCIENCE CHINA
Chemistry

•ARTICLES•

July 2018 Vol.61 No.7: 806–811
https://doi.org/10.1007/s11426-017-9217-4

FeOOH-loaded mesoporous silica nanoparticles as a theranostic platform with pH-responsive MRI contrast enhancement and drug release

Guoming Huang[1], Rui Liu[1], Yuehua Hu[1], Shi-Hua Li[2], Ying Wu[2], Yuan Qiu[1], Jingying Li[1*] & Huang-Hao Yang[2]

[1]*College of Biological Science and Engineering, Fuzhou University, Fuzhou 350116, China;*
[2]*Key Laboratory for Analytical Science of Food Safety and Biology, Ministry of Education, State Key Laboratory of Photocatalysis on Energy and Environment, College of Chemistry, Fuzhou University, Fuzhou 350116, China*

Received November 25, 2017; accepted January 31, 2018; published online March 23, 2018

The development of stimuli-responsive theranostic platforms is of great demand for efficient cancer treatment because they can enhance diagnostic specificity and sensitivity. In this work, we report a pH-responsive theranostic nanoplatform based on FeOOH clusters loaded mesoporous silica nanoparticles (Fe@MSNs). The as-synthesized Fe@MSNs possess activatable T_1 magnetic resonance imaging (MRI) performance that can respond to the acidic microenvironment of solid tumor to turn on T_1 singals by releasing paramagnetic Fe^{3+} ions. The Fe@MSNs are biocompatible without appreciable cytotoxicity. Moreover, the unique mesoporous structure endows the Fe@MSNs with significant advantages to effectively deliver chemotherapeutic drug for inhibiting the growth of solid tumor. We believe that this novel pH-responsive theranostic nanoplatform holds great promise in cancer treatment.

mesoporous silica nanoparticles, magnetic resonance imaging, pH-response, cancer diagnosis, cancer therapy

Citation: Huang G, Liu R, Hu Y, Li SH, Wu Y, Qiu Y, Li J, Yang HH. FeOOH-loaded mesoporous silica nanoparticles as a theranostic platform with pH-responsive MRI contrast enhancement and drug release. *Sci China Chem*, 2018, 61: 806–811, https://doi.org/10.1007/s11426-017-9217-4

1 Introduction

The development of highly specific and sensitive imaging techniques is a long-term goal of disease diagnosis [1–4]. Activatable imaging nanoprobes that generate signals in response to pathological stimuli, such as pH, temperature, and redox potential, have received widespread attention because they can minimize the background signal originating from nontarget tissues [5–8]. Among various imaging techniques, magnetic resonance imaging (MRI) is one of the most powerful medical imaging modalities due to its noninvasive character, deep tissue penetration, and ability to provide images with excellent anatomical details. MRI contrast agents can greatly improve the accuracy and specificity of MRI by enhancing the visibility of the target from the background [9–12]. For example, T_1 contrast agents can shorten the longitudinal relaxation time of the surrounding water protons, resulting in a brighter signal in target region. Paramagnetic metal ions with a large number of unpaired electrons, including Gd^{3+}, Mn^{2+}, and Fe^{3+}, are desirable for T_1 contrast agents. Paramagnetic Gd^{3+}, Mn^{2+}, and Fe^{3+}-based nanomaterials have been broadly developed as T_1 MRI contrast agents [13,14]. For example, Gd_2O_3 nanoparticles, MnO nanoparticles, and ultrasmall Fe_3O_4 nanoparticles have been demonstrated to effectively generate T_1 contrast effects [15–17]. However, these T_1 MRI contrast agents produced signals continuously (so-called "always on"), which lack

*Corresponding author (email: lijingying@fzu.edu.cn)

specificity and sensitivity and fail to response to pathological changes. The exploitation of smart MRI contrast agents that signals only "turned on" under certain conditions is still of great demand.

In recent years, theranostic nanoagents that combinating imaging and therapy within a single nano-formulation have been explosively investigated as next-generation nanomedicine system [18–21]. The specific incorporation of diagnostic and therapeutic functions enables the diagnosis and treatment of diseases to be conductd in a single procedure. Furthermore, theranostic nanosystems can serve as useful tools for real time monitoring biological responses and therapeutic efficacy [22,23]. Unfortunately, conventional MRI contrast agents do not have therapeutic functions. The construction of MRI-guided theranostic nanosystems with stimuli-responsiveness to the tumor microenvironment, such as physiological difference in pH, is highly desired for the development of better cancer therapies. Because of their easy synthesis and unique mesoporous structure, mesoporous silica nanoparticles (MSNs) have been widely utilized in biomedical applications [24,25]. The high specific surface area and large pore volume endow them with significant advantages to act as efficient delivery carriers for various therapeutic agents [26]. More importantly, silica possesses good biocompatibility, which is widely accepted as safe [24]. Therefore, the MSNs hold great promise in the translation from the laboratory to the clinic. In this work, we report a pH-responsive nanoplatform with activable MRI based on MSNs for cancer theranostics (Scheme 1). The MSNs were loaded with Fe^{3+} ions and then treated with a hydrothermal process to form FeOOH clusters within the MSNs. The as-synthesized FeOOH clusters-confined MSNs (Fe@MSNs) can respond to acidic environment and release paramagnetic Fe^{3+} ions, leading to significant T_1 MRI contrast enhancement. Furthermore, the mesoporous structure enables Fe@MSNs to effectively load drug. Therefore, the Fe@MSNs can achieve pH-responsive T_1 contrast enhancement and drug release features simultaneously for cancer theranostics.

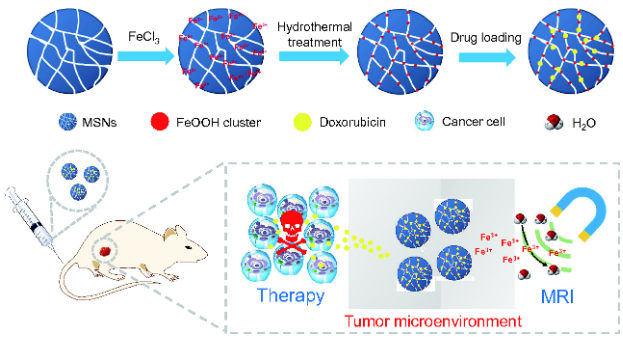

Scheme 1 Schematic illustration of the synthesis and application in serving as a pH-responsive theranostic nanoplatform of Fe@MSNs (color online).

2 Experimental

2.1 Materials

Hexadecyltrimethylammonium chloride (CTAC), triethanolamine (TEA), and tetraethyl orthosilicate (TEOS) were purchased from Sigma-Aldrich (USA). Iron(III) chloride hexahydrate ($FeCl_3·6H_2O$, 99+%) was purchased from Alfa Aesar (USA). Doxorubicin hydrochloride (DOX) was purchased from J&K Scientific (Beijing, China).

2.2 Characterisation

Transmission electron microscopy (TEM) image and energy-dispersive X-ray spectroscopy (EDS) were collected on a Hitachi HT7700 (Japan) at an accelerating voltage of 100 kV. Energy dispersive X-ray (EDX) element mapping analyses were performed on a Tecnai G2 F20 microscope (EFI, USA) at an accelerating voltage of 200 kV. X-ray photoelectron spectroscopy (XPS) was measured on a Thermo escalab 250Xi XPS spectrometer (USA). Dynamic light scattering (DLS) was performed on a Malvern Zetasizer nano ZS instrument (UK). The metal concentration of samples was determined by a XSeries 2 inductively coupled plasma mass spectrometry (ICP-MS) (Thermo Fisher Scientific, USA). Confocal fluorescence microscope imaging was performed on a Nikon A1 CLSM microscope (Japan).

2.3 Synthesis of Fe@MSNs

The MSNs were firstly synthesized according to the previous method [27]. In brief, 2 g of CTAC and 71 μL of TEA were dispersed in 20 mL of water at 95 °C under vigorous stirring for 1 h. Subsequently, 1.5 mL of TEOS was added dropwise and the reaction mixture was stirred for another 1 h. The product was collected by centrifugation and washed with ethanol several times. Finally, the obtained MSNs were extracted for 3 h with methanol solution containing 1 wt% NaCl for several times to remove the CTAC. To load Fe^{3+} ions, the MSNs were dispersed in $FeCl_3$ aqueous solution (1 g mL^{-1}). After stirring for 12 h, the product was collected by centrifugation and washed with water two times. The Fe^{3+} stored MSNs were re-dispersed in water, and the resulting solution was transferred into a Teflon-lined stainless-steel autoclave. After hydrothermal treatment at 150 °C for 3 h, the Fe@MSNs products were collected by centrifugation and washed with deionized water several times.

2.4 *In vitro* MRI

The *in vitro* MRI studies were performed on a 0.5 T NMR120-Analyst NMR system (Niumag Corporation, Shanghai, China). The longitudinal relaxation times (T_1) were measured using an inversion recovery (IR) sequence.

The longitudinal relaxivity (r_1) was determined from the slope of the plot of $1/T_1$ against Fe concentrations ([Fe], mM). T_1-weighted phantom images were acquired using a 2D multi-slice spin-echo (MSE) sequence with the following parameters: TR/TE=100/2 ms, thickness=1 mm, 512×512 matrices, slices=1, and NS=4. For cell imaging, 1×10^7 HeLa cells were incubated with Fe@MSNs (200 μg mL^{-1}) at 37 °C for 2, 6, and 12 h, respectively. Subsequently, the cells were collected and washed with phosphate buffered saline (PBS) three times to remove the free Fe@MSNs. Finally, the cells were concentrated at the button of small tubes by centrifugation for T_1-weighted phantom imaging.

2.5 Drug loading and release

To load the DOX, Fe@MSNs (0.2 mg mL^{-1}) were mixed with DOX solution (200 μg mL^{-1}). After stirring for 48 h at room temperature under dark condition, the DOX loaded Fe@MSNs were collected by centrifugation. The supernatant solution was measured by UV-vis spectrum at 480 nm wavelength to determine the residual DOX content. The loading capacity was calculated by comparing the total amount of DOX before and after loading. To investigate the release of DOX, Fe@MSNs-DOX were dispersed in pH 5.4 citrate buffer or pH 7.4 PBS. At different time points, the supernatant was monitored by UV-Vis spectrum at 480 nm wavelength to determine the release amount of DOX. The standard curve was created by measuring the absorbance at 480 nm wavelength of several DOX samples with known concentrations.

2.6 Cytotoxicity assay

The cytotoxicity of the Fe@MSNs and Fe@MSNs-DOX was evaluated by 3-(4,5-dimethylthiazol-2-y1)-2,5-diphenyltetrazolium bromide (MTT) assay. HeLa cells were firstly seeded into a 96-well plate with a density of 1×10^4 cells/well in RPMI-1640, and incubated in the atmosphere of 5% CO_2 at 37 °C for 24 h. The cells were then incubated with Fe@MSNs or Fe@MSNs-DOX at various concentrations for another 24 h. After that, the culture medium was discarded, and each well was added with 100 μL of new culture medium containing MTT (0.5 mg mL^{-1}) and the plate was incubated for 4 h at 37 °C. Finally, the medium was discarded and each well was added 200 μL dimethyl sulfoxide (DMSO). The OD_{490} value (Abs.) of each well was measured by a SH-1000 Lab microplate reader immediately. The cell viability was calculated from OD_{490} value of experimental group by subtracting that of blank group.

2.7 Blood circulation and tissue biodistribution analyses

Animal experiments were executed in accordance with the Guide for the Care and Use of Laboratory Animals (Ministry of Science and Technology of China, 2006) and were approved by Institutional Animal Care and Use Committee of Fuzhou University. Male BALB/c nude mice (~20 g) were purchased from Shanghai SLAC laboratory Animal Co. Ltd. (China). To induce a solid tumor, murine sarcoma S180 cells (5×10^6 in 100 μL PBS) were injected subcutaneously into the right thigh areas of the mice. The mice were intravenously injected with 100 μL of Fe@MSNs-DOX (535.8 mg Si per kg of mouse body weight). For blood circulation analysis, 50 μL of blood were collected from mice submandibular vein at different time points. To investigate the tissue biodistribution of Fe@MSNs-DOX, the mice were sacrificed 12 h after the injection, and heart, liver, spleen, lung, kidney, and tumor were collected for analyses. The blood and tissue samples were treated with HNO_3-H_2O_2 and NH_4HF_2 digestions, and Si concentration in these samples was measured by ICP-MS.

2.8 *In vivo* MRI

T_1-weighted images of the mice were first collected on a PharmaScan 70/16 US MRI scanner (Bruker, German) without injection. The mice were then intravenously injected with 50 μL of Fe@MSNs-DOX (dosage of 6 mg Fe per kg of mouse body weight). The same slices were further acquired at 2, 8 and 24 h after the injection, respectively. All the images were obtained using a T1 FLASH sequence under the following parameters: TR/TE=500/2.5 ms, FOV=40×40 mm, thickness=0.5 mm. To quantify the contrast enhancement, the signal-to-noise ratio (SNR) was measured by finely analyzing regions of interest (ROIs) of the images, and the contrast enhancement was defined as the increase of SNR after the injection, $\Delta SNR=(SNR_{post}-SNR_{pre})/SNR_{pre}$.

2.9 *In vivo* therapy

To evaluate the anticancer effect of Fe@MSNs-DOX on solid tumor, S180 tumor-bearing nude mice with a tumor diameter of ~6 mm were divided into three groups (five mice per group). The mice of Fe@MSNs-DOX treated group were intravenously injected with 100 μL of Fe@MSNs-DOX (20 mg Fe per kg of mouse body weight). The mice of Fe@MSNs group were intravenously injected with Fe@MSNs with the same dose. The mice of PBS group were intravenously injected with 100 μL of PBS only. The sizes of tumors were measured by a caliper and the tumor volume was calculated according to equation: tumor volume=(tumor length)×(tumor width)^2/2. Relative tumor volumes were calculated as V/V_0 (V was the tumor volume calculated after treatment, while V_0 was the initiated tumor volume before treatment). For hematoxylin and eosin (H&E) staining, tumor bearing mouse was sacrificed 3 d after the treatment,

and the tumor was collected for analysis. The tumor section with thickness of 4 μm was prepared and stained with H&E following the standard protocol.

3 Results and discussion

We firstly synthesized the MSNs according to the previous method [27]. To load Fe^{3+} ions, the as-prepared MSNs were mixed with $FeCl_3$ aqueous solution and stirred overnight. After the centrifugation, yellow products were collected. The colour of the collected MSNs precipitate turned from white to yellow, indicating that the Fe^{3+} ions were successfully stored into the mesoporous of MSNs (Figure S1(a, b), Supporting Information online). The Fe^{3+} ions stored MSNs were re-dispersed in water, and followed with a hydrothermal treatment. The hydrothermal treatment promoted the hydrolysis of Fe^{3+} ions, leading to the formation of FeOOH clusters [28]. The colour of the treated MSNs aqueous solution becoming orange suggested the formation of FeOOH clusters within MSNs (Figure S1(c)). The transmission electron microscopy (TEM) image showed that the as-synthesized Fe@MSNs had a spherical shape, with a diameter of 75.02±6.69 nm (Figure 1(a)). The EDS analysis showed typical peaks of Fe, and the atomic ratio of Si:Fe was determined as about 47.8 (Figure 1(b)). The element mapping analysis of Fe@MSNs revealed that the distribution of Fe in MSNs was homogeneous (Figure S2). The XPS spectrum of Fe@MSNs exhibited typical Fe 2p photoelectron lines. The Fe $2p_{3/2}$ peak was measured at a binding energy of about 711.25 eV, which agrees with the value of that in FeOOH [29], indicating the successful formation of FeOOH within MSNs (Figure 1(c)). The dynamic light scattering analysis presented that the hydrodynamic diameter (HD) of Fe@MSNs was about 106 nm (Figure 1(d)). The mass ratio of Si and Fe in Fe@MSNs determined by ICP-MS was about 26.79.

To investigate the pH-responsive behavior of Fe@MSNs, we dispersed Fe@MSNs in buffer solutions with different pH. We measured the release profiles of Fe^{3+} ions by ICP-MS at different incubation times (Figure 2(a)). The Fe@MSNs showed a slow release of Fe^{3+} ions at pH 7.4 PBS, and only 20.87% of Fe^{3+} ions were released within 24 h. In contrast, a faster release was observed when the Fe@MSNs were dispersed in pH 5.4 citrate buffer. About 63.52% of Fe^{3+} ions were released within 12 h at pH 5.4. Paramagnetic Fe^{3+} ions can shorten the T_1 relaxation time of the surrounding water protons due to their high magnetic moment and long electron spin relaxation time. The pH-triggered release of Fe^{3+} ions capability suggests the potential of Fe@MSNs to serve as an activatable T_1 MRI contrast agent. We then evaluated the T_1 MRI performance of Fe@MSNs under different pH conditions. The r_1 values of Fe@MSNs were first measured on a

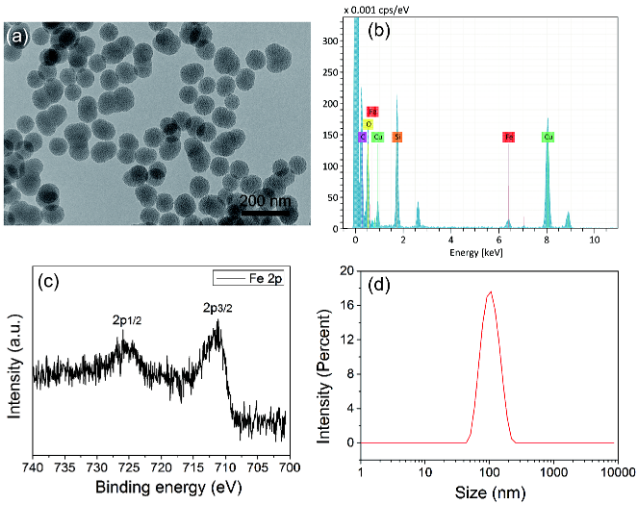

Figure 1 (a) TEM image, (b) EDS pattern, (c) XPS Fe 2p spectrum, and (d) hydrodynamic diameter of the Fe@MSNs (color online).

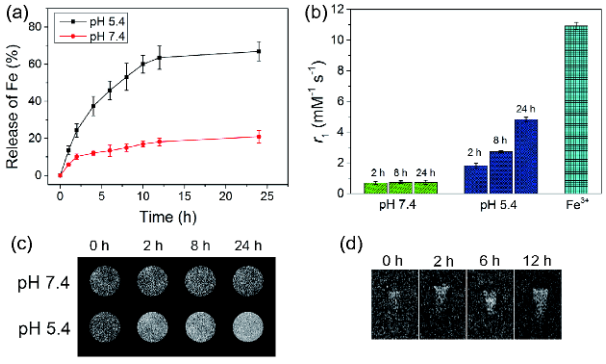

Figure 2 (a) Release profiles of Fe^{3+} ions from Fe@MSNs at pH 5.4 and pH 7.4 (n=3); (b) r_1 values (n=3) and (c) T_1-weighted phantom images of Fe@MSNs dispersed in buffers with different pH for different times ([Fe]=0.4 mM); (d) T_1-weighted images of HeLa cells after incubating with Fe@MSNs for different times (color online).

0.5 T MRI system (Figure 2(b)). The free Fe^{3+} ions ($FeCl_3$ in 5% HNO_3) have an r_1 value of 10.91±0.23 mM^{-1} s^{-1}, confirming that they can shorten the T_1 relaxation time of water protons (Figure 2(b)). The Fe@MSNs showed relatively low r_1 values (~0.71±0.14 mM^{-1} s^{-1}) at pH 7.4, indicating that Fe@MSNs generated little T_1 contrast performance under neutral conditions. However, the r_1 value of Fe@MSNs could significantly increase when the Fe@MSNs were dispersed in pH 5.4 buffer. For example, the r_1 value increased to 4.82±0.13 mM^{-1} s^{-1} at 24 h. This r_1 value is similar to that of commercial Gd contrast agents such as Gd-DTPA and Gd-DOTA (4–5 mM^{-1} s^{-1} at 0.5 T) [19,30]. The acidic environment triggered the Fe@MSNs to release paramagnetic Fe^{3+} ions, leading to the great enhancement in T_1 relaxivity. We further collected the T_1-weighted phantom images of Fe@MSNs at different pH conditions (Figure 2(c)). No appreciable brighten signals were observed in phantom images at pH 7.4, suggesting that Fe@MSNs exhibited little T_1

contrast enhancement at pH 7.4. In contrast, significant brighten signals were observed when Fe@MSNs were dispersed in acidic buffer. This could be ascribed to the release of Fe^{3+} ions triggered by acidic environment. We next tested the pH-responsive contrast performance of Fe@MSNs inside living cells. HeLa cells were incubated with Fe@MSNs and then were collected at different time points for T_1-weighted imaging. Cells can uptake nanoparticles through endocytosis and trap them in endosomes and lysosomes [31]. T_1-weighted imaging of the HeLa cells showed that a gradual enhancement in brighten signals were observed in phantom images with the increase of incubation time, suggesting that the acidic condition of endosomes or lysosomes could trigger Fe@MSNs to release Fe^{3+} ions, therefore resulting in the T_1 contrast enhancement of the cells (Figure 2(d)).

To investigate the capability of Fe@MSNs for drug delivery, we chose clinically approved doxorubicin (DOX) as the model drug. DOX was loaded into the mesoporous of Fe@MSNs at pH 7.4. About 50 wt% DOX was loaded as determined by comparing the total amount of drug before and after loading, and the loading content reached up to 33.3% after the optimization of precursor ratios (Table S1, Supporting Information online). To determine the drug release behavior of Fe@MSNs-DOX, we measured the release amount of DOX at pH 5.4 and 7.4. (Figure 3(a)). The DOX showed a relatively slow release from Fe@MSNs-DOX at pH 7.4, and only 21% DOX was released within 12 h. Interestingly, the release of DOX from Fe@MSNs-DOX was significantly accelerated in the acidic environment, and about 53.7% DOX was released within 12 h at pH 5.4. This acid-sensitive drug release behavior of Fe@MSNs-DOX suggested its great potential for drug delivery. To evaluate the therapeutic efficiency of Fe@MSNs-DOX, we first investigated the cytotoxicity of Fe@MSNs using the tetrazolium-based colorimetric assay (MTT assay). The Fe@MSNs showed no appreciable cytotoxicity on HeLa cells after being incubated with HeLa cells for 24 h, confirming the good biocompatibility of Fe@MSNs (Figure S3). We then assessed the cytotoxicity of Fe@MSNs-DOX. The confocal fluorescence microscope images confirmed the effective intracellular uptake of Fe@MSNs-DOX by HeLa cells after the incubation (Figure S4). Similar to the free DOX, the Fe@MSNs-DOX exhibited dose-dependent cytotoxicity on HeLa cells, indicating that Fe@MSNs-DOX could effectively inhibit the growth of cancer cells (Figure 3 (b)). The enhanced cellular uptake of Fe@MSNs-DOX could lead to the high accumulation of DOX within cancer cells.

Encouraged by the *in vitro* results, we further investigated the *in vivo* pH-triggered MRI and therapy performance of Fe@MSNs-DOX on S180 tumor bearing BALB/c nude mice. We first investigated the blood circulation behavior and biodistribution of Fe@MSNs-DOX after the intravenous injection. The blood circulation analysis showed that Fe@MSNs-DOX circulated in blood over a span of 12 h (Figure S5). The biodistribution analysis confirmed that Fe@MSNs-DOX could effectively accumulate in tumor (Figure S6). T_1-weighted images of the mice were then collected at different time points. Tumor region showed gradual brightening signals with increasing time after the administration of Fe@MSNs-DOX (Figure 4(a)), confirming that the Fe@MSNs-DOX could accumulate in tumor via EPR effect. To quantify these T_1 signal enhancements, we calculated the signal-to-noise ratio (SNR) by analyzing the measurement region of interest (MROI) in tumor area. The contrast enhancement was defined as the change of SNR, $\Delta SNR = (SNR_{post} - SNR_{pre})/SNR_{pre}$. The calculated ΔSNR values were 18.8%±11.1%, 60.5%±8.1%, 7.4%±4.1% at 2, 8 and 24 h after the injecion, respectively (Figure 4(b)). These time-dependent T_1 signal changes confirmed that the acidic microenvironment of tumor could stimulate the Fe@MSNs-DOX to release Fe^{3+} ions, leading to the shortening effect of longitudinal relaxation in tumor region. We further evaluate the chemotherapy performance of Fe@MSNs-DOX by monitoring the growth of solid tumor. Notably, the Fe@MSNs-DOX showed an obvious inhibitory effect on the growth of S180 tumor, suggesting the outstanding *in vivo* therapeutic performance of Fe@MSNs-DOX (Figure 4(c)).

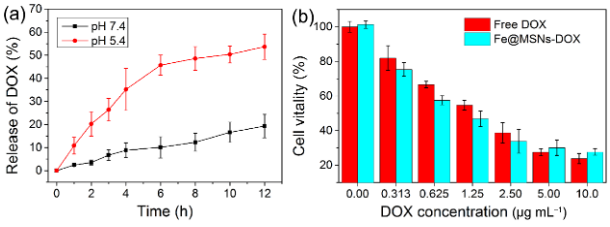

Figure 3 (a) Release profiles of DOX from Fe@MSNs-DOX in different pH buffers (n=3); (b) cell viability of HeLa cells after being incubated with free DOX or Fe@MSNs-DOX for 24 h, respectively (n=3) (color online).

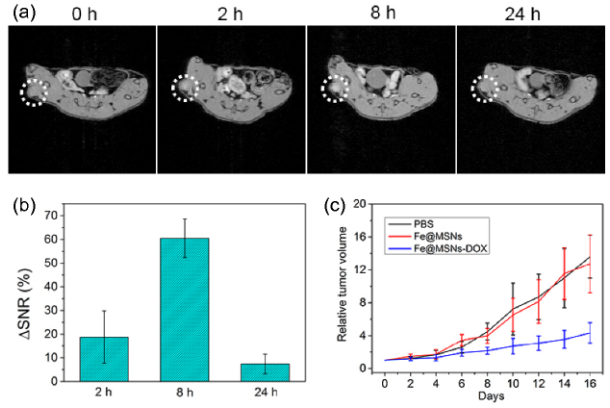

Figure 4 (a) T_1-weighted images and (b) quantificational analysis of signal-to-noise changes (ΔSNR) of mice at different time points after the injection of Fe@MSNs-DOX (n=3). The regions of tumor are indicated by dash lines. (c) Tumor growth curves of S180 tumor-bearing mice after different treatments (n=5) (color online).

The H&E staining of tumor section revealed the necrosis that tumor cells were irregularly shaped with shrinking cell nucleus, confirming the therapeutic effect of Fe@MSNs-DOX (Figure S7). The body weight of the mice was also monitored during the treatment. No significant weight drops were observed, suggesting the low toxicity of the treatments (Figure S8).

4 Conclusions

In conclusion, we have successfully synthesized Fe@MSNs and applied them as a pH-responsive nanoplatform for cancer theranostics. The Fe@MSNs can respond to the acidic microenvironment of tumor, triggering the release of paramagnetic Fe^{3+} ions to switch on the T_1 MRI singals in the tumor area. Furthermore, the mesoporous structure of Fe@MSNs makes them efficient drug carriers to deliver chemotherapeutic drug for cancer treatment. We believe that this biocompatible pH-responsive theranostic nanoplatform holds the great potential for further clinical translations and applications.

Acknowledgements This work was supported by the National Natural Science Foundation of China (81501461, 21635002) and the Open Research Fund for Expensive Instrument Testing of Fuzhou University (2017T026, 2017T028).

Conflict of interest The authors declare that they have no conflict of interest.

Supporting information The supporting information is available online at http://chem.scichina.com and http://link.springer.com/journal/11426. The supporting materials are published as submitted, without typesetting or editing. The responsibility for scientific accuracy and content remains entirely with the authors.

1 Weissleder R, Pittet MJ. *Nature*, 2008, 452: 580–589
2 Smith BR, Gambhir SS. *Chem Rev*, 2017, 117: 901–986
3 Zhan S, Lou X, Xia F. *Sci China Chem*, 2017, 60: 1267–1276
4 Gao Z, Deng S, Li J, Wang K, Li J, Wang L, Fan C. *Sci China Chem*, 2017, 60: 1305–1309
5 Li J, Cheng F, Huang H, Li L, Zhu JJ. *Chem Soc Rev*, 2015, 44: 7855–7880
6 Urano Y, Asanuma D, Hama Y, Koyama Y, Barrett T, Kamiya M, Nagano T, Watanabe T, Hasegawa A, Choyke PL, Kobayashi H. *Nat Med*, 2009, 15: 104–109
7 Huang G, Zhang KL, Chen S, Li SH, Wang LL, Wang LP, Liu R, Gao J, Yang HH. *J Mater Chem B*, 2017, 5: 3629–3633
8 Zhang M, He K, Wu J, Li N, Yuan J, Zhou W, Ye Z, Li Z, Xiao H, Lv Z, Zhang Y, Fang X. *Sci China Chem*, 2017, 60: 1310–1317
9 Shin TH, Choi Y, Kim S, Cheon J. *Chem Soc Rev*, 2015, 44: 4501–4516
10 Zhou Z, Bai R, Munasinghe J, Shen Z, Nie L, Chen X. *ACS Nano*, 2017, 11: 5227–5232
11 Huang G, Hu J, Zhang H, Zhou Z, Chi X, Gao J. *Nanoscale*, 2014, 6: 726–730
12 Zhang KL, Zhou J, Zhou H, Wu Y, Liu R, Wang LL, Lin WW, Huang G, Yang HH. *ACS Appl Mater Interfaces*, 2017, 9: 30502–30509
13 Hu F, Zhao YS. *Nanoscale*, 2012, 4: 6235–6243
14 Huang G, Li H, Chen J, Zhao Z, Yang L, Chi X, Chen Z, Wang X, Gao J. *Nanoscale*, 2014, 6: 10404–10412
15 Park JY, Baek MJ, Choi ES, Woo S, Kim JH, Kim TJ, Jung JC, Chae KS, Chang Y, Lee GH. *ACS Nano*, 2009, 3: 3663–3669
16 Na HB, Lee JH, An K, Park YI, Park M, Lee IS, Nam DH, Kim ST, Kim SH, Kim SW, Lim KH, Kim KS, Kim SO, Hyeon T. *Angew Chem Int Ed*, 2007, 46: 5397–5401
17 Kim BH, Lee N, Kim H, An K, Park YI, Choi Y, Shin K, Lee Y, Kwon SG, Na HB, Park JG, Ahn TY, Kim YW, Moon WK, Choi SH, Hyeon T. *J Am Chem Soc*, 2011, 133: 12624–12631
18 Choi KY, Liu G, Lee S, Chen X. *Nanoscale*, 2012, 4: 330–342
19 Guo T, Lin Y, Li Z, Chen S, Huang G, Lin H, Wang J, Liu G, Yang HH. *Nanoscale*, 2017, 9: 56–61
20 Song XR, Yu SX, Jin GX, Wang X, Chen J, Li J, Liu G, Yang HH. *Small*, 2016, 12: 1506–1513
21 Huang G, Zhu X, Li H, Wang L, Chi X, Chen J, Wang X, Chen Z, Gao J. *Nanoscale*, 2015, 7: 2667–2675
22 Terreno E, Uggeri F, Aime S. *J Control Release*, 2012, 161: 328–337
23 Zhao Z, Wang X, Zhang Z, Zhang H, Liu H, Zhu X, Li H, Chi X, Yin Z, Gao J. *ACS Nano*, 2015, 9: 2749–2759
24 Tang F, Li L, Chen D. *Adv Mater*, 2012, 24: 1504–1534
25 Wen J, Yan H, Xia P, Xu Y, Li H, Sun S. *Sci China Chem*, 2017, 60: 799–805
26 Yang P, Gai S, Lin J. *Chem Soc Rev*, 2012, 41: 3679–3698
27 Pan L, He Q, Liu J, Chen Y, Ma M, Zhang L, Shi J. *J Am Chem Soc*, 2012, 134: 5722–5725
28 Qu Q, Yang S, Feng X. *Adv Mater*, 2011, 23: 5574–5580
29 Brion D. *Appl Surf Sci*, 1980, 5: 133–152
30 Wang L, Zhu X, Tang X, Wu C, Zhou Z, Sun C, Deng SL, Ai H, Gao J. *Chem Commun*, 2015, 51: 4390–4393
31 Zhao F, Zhao Y, Liu Y, Chang X, Chen C, Zhao Y. *Small*, 2011, 7: 1322–1337